The Astrophysical Journal Supplement Series, 225:21 (11pp), 2016 August doi:10.3847/0067-0049/225/2/21

THE INFLOW SIGNATURE TOWARD DIFFERENT EVOLUTIONARY PHASES OF MASSIVE STAR FORMATION

Mihwa Jin[1], Jeong-Eun Lee[1], Kee-Tae Kim[2], and Neal J. Evans II[3]
[1] School of Space Research, Kyung Hee University, 1732, Deogyeong-daero, Giheung-gu, Yongin-si, Gyeonggi-do, 17104, Korea; mihwajin.sf@gmail.com, jeongeun.lee@khu.ac.kr
[2] Korea Astronomy and Space Science Institute, 776 Daedeokdae-ro, Yuseong-gu, Daejeon 34055, Korea; ktkim@kasi.re.kr
[3] Department of Astronomy, University of Texas at Austin, 1 University Station, C1400, Austin, Texas 78712-0259, USA; nje@astro.as.utexas.edu
Received 2015 October 22; revised 2016 June 7; accepted 2016 June 21; published 2016 August 11

ABSTRACT

We analyze both HCN $J = 1$–0 and HNC $J = 1$–0 line profiles to study the inflow motions in different evolutionary stages of massive star formation: 54 infrared dark clouds (IRDCs), 69 high-mass protostellar objects (HMPOs), and 54 ultra-compact H II regions (UCHIIs). Inflow asymmetry in the HCN spectra seems to be prevalent throughout all the three evolutionary phases, with IRDCs showing the largest excess in the blue profile. In the case of the HNC spectra, the prevalence of blue sources does not appear, apart from for IRDCs. We suggest that this line is not appropriate to trace the inflow motion in the evolved stages of massive star formation, because the abundance of HNC decreases at high temperatures. This result highlights the importance of considering chemistry in dynamics studies of massive star-forming regions. The fact that the IRDCs show the highest blue excess in both transitions indicates that the most active inflow occurs in the early phase of star formation, i.e., in the IRDC phase rather than in the later phases. However, mass is still inflowing onto some UCHIIs. We also find that the absorption dips of the HNC spectra in six out of seven blue sources are redshifted relative to their systemic velocities. These redshifted absorption dips may indicate global collapse candidates, although mapping observations with better resolution are needed to examine this feature in more detail.

Key words: stars: formation

1. INTRODUCTION

Massive stars are considered to be decisive players in the physical and chemical evolution of galaxies, injecting energetic feedback into their surroundings. In recent years, many studies have tried to examine the formation mechanism of high-mass stars, suggesting an evolutionary sequence of massive star formation as follows. First, the formation of massive stars begins in an infrared dark cloud (IRDC) identified as dark extinction features against the bright Galactic mid-infrared background (Egan et al. 1998; Simon et al. 2006a). Their cold ($\lesssim$25 K) and dense ($\gtrsim 10^5$ cm^{-3}) properties and strong (sub)millimeter emissions (e.g., Rathborne et al. 2006) suggest the regions as ideal birth-places for massive stars. Central condensation then begins heating its environment, evolving to become a high-mass protostellar object (HMPO). They are luminous infrared point-like sources ($L_{\rm bol} \geqslant 10^3\ L_{\odot}$) without associated radio continuum emission (Molinari et al. 1996, 2000; Beuther et al. 2002; Sridharan et al. 2002). This protostar continues to gain mass and evolves to produce UV photons, ionizing the gas, becoming an ultra-compact H II region (UCHII). UCHIIs are very small ($D \lesssim$ 0.1 pc), dense ($n_{\rm e} \gtrsim 10^4$ cm^{-3}), and bright (EM $\gtrsim 10^7$ pc cm^{-6}) ionized regions (Wood & Churchwell 1989; Kurtz et al. 1994; Kim & Koo 2001). These objects are considered to represent the childhood of H II regions.

Nevertheless, the formation mechanism for the massive stars is still under debate. There are two competing theories describing massive star formation: turbulent core accretion and competitive accretion (McKee & Ostriker 2007; Zinnecker & Yorke 2007; Bodenheimer 2011). In the turbulent core accretion model, high-mass cloud cores form from a much larger molecular cloud clump, which is supported by quasi-virialized turbulent flows. The material that ends up as stars can be essentially determined by the process of fragmentation of the cloud clump because the cores are almost non-interacting and the remainder of the clump seldom affects the inflowing process (McKee & Tan 2003). This scenario explains well an initial mass function similar to a core mass function, which is consistent with observations (Motte et al. 1998; Beuther & Schilke 2004; Krumholz & Tan 2007).

In the competitive accretion model, star formation is regulated by the global collapse of a much larger cloud, initially containing gas of several thousand $M_{\odot}$. The material that ends up as stars is gathered during the star formation process from various parts of the parent cloud. The cores compete for the remaining gas and there are strong interactions among them. This scenario predicts that massive stars form at the cluster center where more massive inflow can occur than in the outer regions (Bonnell et al. 2001; Krumholz & Bonnell 2009).

Regardless of which mechanism is at work, gravitational inflow is a key process to initiate star formation and to control the evolution of densities in the protostellar envelope. Therefore, characterizing this inflow process is important for a better understanding of high-mass star formation. One observational signature of inflow motion is a "blue profile," a general prediction for a cloud collapsing model (e.g., Shu 1977). This blue profile is an asymmetric line feature that appears in an optically thick line profile with a self-absorption dip and a stronger blue peak than red peak. The emission of the optically thin line peaks near the absorption dip of the optically thick line.

There have been many attempts to examine the inflow signature in massive star-forming regions in recent years. After Wu & Evans (2003) found statistically significant blue excess (the number of blue profile minus that of red profile in units of the total number of samples) in the blue profile in the HCN

$J = 3$–2 line toward the early phase of H II regions where star-forming activity still appears, the number of studies has been increasing steadily. For example, Reiter et al. (2011a) carried out HCO^+ $J = 3$–2 line observations toward similar regions as Wu & Evans (2003). They noted that every source with blue asymmetry in the HCO^+ $J = 3$–2 line also had a blue profile in the HCN $J = 3$–2 line, and confirmed that the HCN $J = 3$–2 line is a better inflow tracer. Rygl et al. (2013) performed HCO^+ $J = 1$–0, 4–3, and CO $J = 3$–2 line observations toward a sample of clumps in clouds with high extinctions, and they concluded that among the three transitions, the HCO^+ $J = 1$–0 line is the most sensitive for detecting inflowing motions. In addition, Fuller et al. (2005) reported significant excess of blue profiles toward HMPOs in the HCO^+ $J = 1$–0, 3–2, and 4-3 transitions, and H_2CO 2_{12}–1_{11} line.

In addition, there have been several previous studies dealing with the evolutionary tendencies of inflow motion. For example, Wu et al. (2007) showed a dramatic increase of blue excess in the HCO^+ $J = 1$–0 line with evolution from HMPOs to UCHIIs. Other studies have found different results. Purcell et al. (2006) revealed equal numbers of red and blue profiles of the HCO^+ $J = 1$–0 line toward HMPOs and UCHIIs, and only found blue excess in IRDCs, indicating active inflow motion occurring in the early phase of star formation. Recently, an extensive inflow survey toward 405 compact sources classified into prestellar, protostellar, and UCHII regions was performed in the HCO^+ $J = 1$–0 and HNC $J = 1$–0 lines (He et al. 2015). They suggested that the HCO^+ $J = 1$–0 line is better for tracing inward motion and found that the blue excess declines with evolutionary stage. With a higher transition of HCO^+, the opposite tendency appears. In the HCO^+ $J = 4$–3 study by Klaassen et al. (2012), 12 out of 22 UCHIIs showed a blue asymmetric line profile while only three blue sources were detected among 12 HMPOs. They attribute this lower occurrence of blue profiles in the HMPOs to the beam dilution effect.

Apart from the study of Wu et al. (2007), all of these results regarding the HCO^+ $J = 1$–0 line can be summarized as follows. (1) The HCO^+ $J = 1$–0 transition is likely to be the most sensitive inflow tracer. (2) The blue excess measured with this line intensity decreases with evolution of the massive star-forming regions, suggesting that the younger the sources are, the easier it is to detect inflow with this tracer. (3) This observed trend, however, can appear different with higher transition lines.

Many of the above studies mainly used the HCO^+ transitions as an inflow tracer or dealt with limited phases of massive star formation, however, different line transitions at different molecular species must be tested because inflow could be associated with various excitation conditions. In this study, we search for inflow candidates toward various evolutionary stages related to massive star formation (IRDCs, HMPOs, and UCHIIs) using the HCN and HNC $J = 1$–0 lines. This paper is organized as follows. The details of the source selection and observations are provided in Section 2. The analyses for asymmetric profiles are presented in Section 3. The discussion for inflow candidates is provided in Section 4. The main results are summarized in Section 5.

2. OBSERVATION

2.1. Target Selection

After Rathborne et al. (2006) identified 190 compact cores in the 1.2 mm continuum images of the 38 darkest IRDCs, Chambers et al. (2009) classified them as "quiescent" prestellar cores (qIRDCc) and "active" protostellar cores (aIRDCc). aIRDCc show both 4.5 and 24 μm infrared emission, which is the signature of star-forming activities, while qIRDCc contain neither emission. We adopted 19 qIRDCc and 35 aIRDCc from the catalog of Chambers et al. (2009) as our IRDC targets. We selected 69 HMPOs from the catalogs of Sridharan et al. (2002) and Molinari et al. (1996), and 54 UCHIIs from the catalogs of Wood & Churchwell (1989) and Kurtz et al. (1994). The details of selection criteria are provided in Jin et al. (2015). Consequently, our sample consists of 54 IRDCs (19 qIRDCc and 35 aIRDCc), 69 HMPOs, and 54 UCHIIs.

Table 1
Observed Lines

Molecule	Transition	ν (MHz)	μ (D)	S_{ul}[a]
HCN	$J = 1$–0, $F = 2$–1	88630.42	2.99[b]	3
	$J = 1$–0, $F = 1$–1	88631.85	⋯	5
	$J = 1$–0, $F = 0$–1	88633.94	⋯	1
$H^{13}CN$	$J = 1$–0, $F = 2$–1	86338.77	2.99[b]	3
	$J = 1$–0, $F = 1$–1	86340.18	⋯	5
	$J = 1$–0, $F = 0$–1	86342.27	⋯	1
HNC	$J = 1$–0	90663.57	3.05[c]	⋯
$HN^{13}C$	$J = 1$–0	87090.85	3.05[c]	⋯

Notes.
[a] Relative weights of the hyperfine components.
[b] Bhattacharya & Gordy (1960).
[c] Blackman et al. (1976).

2.2. Observations

The $J = 1$–0 transitions of HCN and HNC and their isotopic lines (Table 1) were observed in 2012–2013 using the Korean VLBI Network (KVN) 21 m telescope at the Yonsei and Ulsan stations (Kim et al. 2011; Lee et al. 2011). The main-beam efficiencies are 0.43 and 0.37 for the KVN Yonsei and Ulsan telescopes, respectively, and the beam sizes of both telescopes are 32″. All the lines were observed in position switching mode and their intensities were calibrated on the T_A^* scale by the standard chopper wheel method. The focus and pointing were adjusted by observing strong SiO maser sources every one to two hours. The system temperature ranged from 170 to 280 K. The rest frequencies, dipole moments, and relative weights of the hyperfine components of the observed lines are summarized in Table 1. All spectra were reduced using CLASS in the GILDAS software package, and the reduced line spectra have a velocity resolution of 0.21 km s^{-1}.

3. ANALYSIS AND RESULTS

To select sources for analysis of inflow signatures, we first use a 3σ-detection criterion for each line. Then, some sources are excluded by eye if they are suspected to have multiple velocity components in a line of sight. Specifically, eight IRDC cores are excluded in the analysis of HCN $J = 1$–0. The hyperfine components are strongly self-absorbed and blended into each other, making it difficult for the lines to be exploited in the inflow analysis. In addition, there are additional emission components that cannot be solely explained by the combination of self-absorption and line blending effects in some sources. Finally, 12 IRDCs, 26 HMPOs, and 23 UCHIIs are selected for

Table 2
Source Information

Classification	Source Name	R.A. J(2000.0)	Decl. J(2000.0)	l (°)	b (°)	D_{far} (kpc)	D_{near} (kpc)	Inflow Tracer
qIRDCc	G028.37_MM9	18:42:46.7	−04:04:08	28.32	0.07	5.0	⋯	HCN, HNC
	G031.97_MM9	18:49:31.6	−00:46:30	32.02	0.07	6.9	⋯	HNC
	G035.39_MM5	18:57:08.8	+02:08:09	35.48	−0.30	2.9	⋯	HCN, HNC
aIRDCc	G015.31_MM3	18:18:45.3	−15:41:58	15.28	−0.09	3.2	⋯	HNC
	G022.35_MM1	18:30:24.4	−09:10:34	22.38	0.45	4.3	⋯	HCN
	G023.60_MM1	18:34:11.6	−08:19:06	23.57	0.01	3.9	⋯	HNC
	G023.60_MM6	18:34:18.2	−08:18:52	23.59	−0.01	3.9	⋯	HNC
	G024.60_MM1	18:35:40.2	−07:18:37	24.63	0.15	3.7	⋯	HNC
	G028.37_MM4	18:42:50.7	−04:03:15	28.34	0.06	5.0	⋯	HNC
	G028.37_MM6	18:42:49.0	−04:02:23	28.36	0.07	5.0	⋯	HNC
	G030.97_MM1	18:48:21.6	−01:48:27	30.97	−0.14	5.1	⋯	HCN, HNC
	G031.97_MM1	18:49:36.3	−00:45:45	32.04	0.06	6.9	⋯	HCN, HNC
	G031.97_MM8	18:49:29.1	−00:48:12	32.00	0.07	6.9	⋯	HNC
	G033.69_MM4	18:52:56.4	+00:43:08	33.74	0.00	7.1	⋯	HCN, HNC
	G033.69_MM5	18:52:47.8	+00:36:47	33.63	−0.02	7.1	⋯	HCN, HNC
	G034.43_MM1	18:53:18.0	+01:25:24	34.41	0.24	3.7	⋯	HNC
	G034.43_MM3	18:53:20.4	+01:28:23	34.46	0.25	3.7	⋯	HNC
	G034.43_MM4	18:53:19.0	+01:24:08	34.39	0.22	3.7	⋯	HCN, HNC
	G035.39_MM7	18:57:08.1	+02:10:50	35.52	−0.27	2.9	⋯	HCN
	G035.59_MM3	18:57:11.6	+02:16:08	35.61	−0.24	2.9	⋯	HNC
	G038.95_MM3	19:04:07.4	+05:09:44	38.97	−0.46	2.7	⋯	HNC
	G038.95_MM4	19:04:00.6	+05:09:06	38.95	−0.44	2.7	⋯	HNC
	G048.65_MM1	19:21:49.7	+13:49:30	48.67	−0.30	2.5	⋯	HCN, HNC
	G048.65_MM2	19:21:47.6	+13:49:22	48.66	−0.30	2.5	⋯	HNC
	G053.25_MM4	19:29:34.5	+18:01:39	53.25	0.05	1.9	⋯	HCN, HNC
	G053.25_MM6	19:29:31.5	+17:59:50	53.22	0.05	1.9	⋯	HCN, HNC
	G053.31_MM2	19:29:42.1	+18:03:57	53.30	0.05	2.0	⋯	HNC
HMPO	IRAS 00117+6412	00:14:27.7	+64:28:46	118.96	1.89	1.8	⋯	HCN
	IRAS 05358+3543	05:39:10.4	+35:45:19	173.48	2.43	1.8	⋯	HCN, HNC
	IRAS 05373+2349	05:40:24.4	+23:50:54	183.72	−3.66	1.2	⋯	HCN, HNC
	IRAS 18024-2119	18:05:25.4	−21:19:41	8.83	−0.03	0.1	⋯	HNC
	IRAS 18089-1732	18:11:51.3	−17:31:28	12.89	0.49	13.0	3.6	HNC
	IRAS 18102-1800	18:13:12.2	−17:59:35	12.63	−0.02	14.0	2.6	HNC
	IRAS 18144-1723	18:17:24.4	−17:22:13	13.66	−0.60	4.3	⋯	HNC
	IRAS 18151-1208	18:17:57.1	−12:07:22	18.34	1.77	3.0	⋯	HCN, HNC
	IRAS 18162-1612	18:19:07.5	−16:11:21	14.89	−0.40	4.9	⋯	HNC
	IRAS 18182-1433	18:21:07.9	−14:31:53	16.58	−0.05	11.8	4.5	HCN, HNC
	IRAS 18223-1243	18:25:10.9	−12:42:17	18.66	−0.06	12.4	3.7	HCN, HNC
	IRAS 18264-1152	18:29:14.3	−11:50:26	19.88	−0.53	12.5	3.5	HCN, HNC
	IRAS 18290-0924	18:31:44.8	−09:22:09	22.36	0.06	10.5	5.3	HNC
	IRAS 18308-0841	18:33:31.9	−08:39:17	23.20	0.00	10.7	4.9	HCN
	IRAS 18310-0825	18:33:47.2	−08:23:35	23.46	0.07	10.4	5.2	HNC
	IRAS 18345-0641	18:37:16.8	−06:38:32	25.41	0.10	9.5	⋯	HNC
	IRAS 18440-0148	18:46:36.3	−01:45:23	30.82	0.27	8.3	⋯	HCN, HNC
	IRAS 18445-0222	18:47:10.8	−02:19:06	30.38	−0.11	9.4	5.3	HCN
	IRAS 18447-0229	18:47:23.7	−02:25:55	30.31	−0.21	8.2	6.6	HCN
	IRAS 18470-0044	18:49:36.7	−00:41:05	32.11	0.09	8.2	⋯	HCN, HNC
	IRAS 18488+0000	18:51:24.8	+00:04:19	32.99	0.04	8.9	5.4	HNC
	IRAS 18511+0146	18:53:38.1	+01:50:27	34.82	0.35	3.9	⋯	HNC
	IRAS 18527+0301	18:55:16.5	+03:05:07	36.11	0.55	5.26	⋯	HCN
	IRAS 18530+0215	18:55:34.2	+02:19:08	35.47	0.14	8.7	5.1	HCN, HNC
	IRAS 19012+0536	19:03:45.1	+05:40:40	39.39	−0.14	8.6	4.6	HCN
	IRAS 19035+0641	19:06:01.1	+06:46:35	40.62	−0.14	2.2	⋯	HCN
	IRAS 19220+1432	19:24:19.7	+14:38:03	49.67	−0.46	5.5	⋯	HNC
	IRAS 19410+2336	19:43:11.4	+23:44:06	59.78	0.06	6.4	2.1	HCN
	IRAS 19411+2306	19:43:18.1	+23:13:59	59.36	−0.21	5.8	2.9	HCN, HNC
	IRAS 19413+2332	19:43:28.9	+23:40:04	59.76	−0.03	6.8	1.8	HCN
	IRAS 20126+4104	20:14:26.0	+41:13:32	78.12	3.63	1.7	⋯	HCN, HNC
	IRAS 20216+4107	20:23:23.8	+41:17:40	79.12	2.28	1.7	⋯	HCN, HNC
	IRAS 20293+3952	20:31:10.7	+40:03:10	78.98	0.36	2.0	1.3	HNC
	IRAS 20343+4129	20:36:07.1	+41:40:01	80.83	0.57	1.4	⋯	HCN, HNC
	IRAS 22134+5834	22:15:09.1	+58:49:09	103.88	1.86	2.6	⋯	HCN, HNC
	IRAS 22198+6336	22:21:27.6	+63:51:42	107.30	5.64	1.3	⋯	HCN, HNC

Table 2
(Continued)

Classification	Source Name	R.A. J(2000.0)	Decl. J(2000.0)	l (°)	b (°)	D_{far} (kpc)	D_{near} (kpc)	Inflow Tracer
	IRAS 23033+5951	23:05:25.7	+60:08:08	110.09	−0.07	3.5	···	HCN, HNC
	IRAS 23140+6121	23:16:11.7	+61:37:45	111.87	0.82	6.44	···	HCN
UCHII	IRAS 02232+6138	02:27:01.0	+61:52:14	133.94	1.06	3.0	···	HCN, HNC
	IRAS 02575+6017	03:01:32.3	+60:29:12	138.30	1.56	3.8	···	HCN, HNC
	IRAS 03035+5819	03:07:25.6	+58:30:52	139.91	0.20	4.2	···	HCN
	IRAS 05393-0156	05:41:49.5	−01:55:17	206.56	−16.34	0.5	···	HNC
	IRAS 06053-0622	06:07:46.6	−06:22:59	213.70	−12.60	10.8	···	HCN
	IRAS 06056+2131	06:08:41.0	+21:31:01	189.03	0.78	0.8	···	HCN, HNC
	IRAS 06058+2138	06:08:54.1	+21:38:25	188.95	0.89	2.2	···	HCN, HNC
	IRAS 06061+2151	06:09:07.8	+21:50:39	188.80	1.03	4.1	···	HCN
	IRAS 06084-0611	06:10:51.0	−06:11:54	213.88	−11.84	1.0	···	HCN, HNC
	IRAS 06099+1800	06:12:53.3	+17:59:22	192.60	−0.05	2.5	···	HCN, HNC
	IRAS 17574-2403	18:00:30.4	−24:04:00	5.89	−0.39	2.0	···	HNC
	IRAS 17599-2148	18:03:00.4	−21:48:05	8.14	0.23	4.2	···	HCN, HNC
	IRAS 18032-2137	18:06:19.0	−21:37:32	8.67	−0.36	4.8	···	HNC
	IRAS 18075-1956	18:10:23.5	−19:56:15	10.61	−0.37	4.8	···	HCN, HNC
	IRAS 18100-1854	18:14:01.1	−18:53:24	11.94	−0.62	5.2	···	HNC
	IRAS 18162-2048	18:19:11.9	−20:47:34	10.84	−2.59	1.9	···	HCN, HNC
	IRAS 18174-1612	18:20:24.8	−16:11:35	15.03	−0.68	2.1	···	HCN
	IRAS 18317-0757	18:34:24.9	−07:54:48	23.95	0.15	6.0	···	HCN
	IRAS 18403-0417	18:42:58.2	−04:14:00	28.20	−0.05	9.1	···	HNC
	IRAS 18434-0242	18:46:03.9	−02:39:22	29.96	−0.03	7.4	···	HCN, HNC
	IRAS 18469-0132	18:49:34.7	−01:29:08	31.40	−0.26	7.3	···	HCN
	IRAS 19095+0930	19:11:53.3	+09:35:46	43.79	−0.13	9.0	···	HNC
	IRAS 20081+3122	20:10:09.1	+31:31:34	69.54	−0.98	3.0	···	HNC
	IRAS 20255+3712	20:27:26.6	+37:22:48	76.38	−0.62	1.0	···	HCN, HNC
	IRAS 20178+4046	20:19:39.3	+40:56:30	78.44	2.66	3.3	···	HCN, HNC
	IRAS 20350+4126	20:36:52.6	+41:36:32	80.87	0.42	2.1	···	HCN, HNC
	IRAS 22176+6303	22:19:18.2	+63:18:46	106.80	5.31	0.9	···	HCN, HNC
	IRAS 22543+6145	22:56:19.1	+62:01:57	109.87	2.12	0.7	···	HCN, HNC
	IRAS 23133+6050	23:15:31.5	+61:07:09	111.61	0.37	5.2	···	HCN
	IRAS 23138+5945	23:16:04.8	+60:02:00	111.28	−0.66	2.5	···	HCN, HNC

Note. Kinetic distances are quoted from Simon et al. (2006b) (IRDCs), Beuther et al. (2002), Molinari et al. (1996) (HMPOs), and Thompson et al. (2006) and references therein (UCHIIs). If the distance ambiguity is resolved, only far and no near distance is noted.

the HCN and $H^{13}CN$ line analysis while 25 IRDCs, 28 HMPOs, and 23 UCHIIs are selected for the analysis of the HNC and $HN^{13}C$ lines. The information for the sources selected for analysis is listed in Table 2.

According to Wu & Evans (2003), the inflow proceeds at a relatively low velocity so that its observational signature can be easily masked by other mechanisms or a beam dilution effect. However, all our samples that are listed in the SCUBA legacy catalog have larger effective radii than half of our beam size in the 850 μm continuum (Di Francesco et al. 2008; Jin et al. 2015), indicating that the emission is not likely beam-diluted. The HCN and HNC line emissions are known to be well correlated with the dust emission (Wu et al. 2010; Reiter et al. 2011b).

The general signature of inflow is the so called "blue profile." This is an asymmetric line feature with a self-absorption dip where the blue peak is stronger than the red peak, while an optically thin line must peak near the dip of the optically thick line. In this case, the ratio of the blue peak to the red peak ($T(B)/T(R)$) can be one measure for the line asymmetry. However, depending on the opacity of the line, the blue profiles can show other features, for example, a single blue peak with a red shoulder or a blue-skewed single peak. Figures 1–2 show the various features of blue profiles in the HCN and HNC $J = 1$–0 lines, respectively, ranging from a clearly self-absorbed blue profile to a blue-skewed profile.

In low-mass star-forming regions, Mardones et al. (1997) have suggested δv as an alternative measure of the blue profile for these blue-skewed lines, which is defined as a difference between the line central velocity of an optically thick line (v_{thick}) and that of an optically thin line (v_{thin}), in units of the line width of the optically thin line (Δv_{thin})

$$\delta v = \frac{v_{thick} - v_{thin}}{\Delta v_{thin}}. \quad (1)$$

A line can be identified as blue/red profile if the difference between v_{thick} and v_{thin} is greater than a quarter of Δv_{thin}. That is, a blue profile would have $\delta v < -0.25$ while a red profile would have $\delta v > 0.25$ (Mardones et al. 1997). However, it is important to note that adopting the same boundaries on δv for these high-mass objects actually demands a larger velocity shift than for the low-mass sources because the molecular lines toward these high-mass samples are significantly broader (Fuller et al. 2005).

We measured the line asymmetries of all the detected sources using the δv analysis under the assumption that both the $H^{13}CN$ and $HN^{13}C$ lines are optically thin. The optical depth for each line was obtained by adopting the values of Jin et al. (2015) or by following the same analysis described therein. The

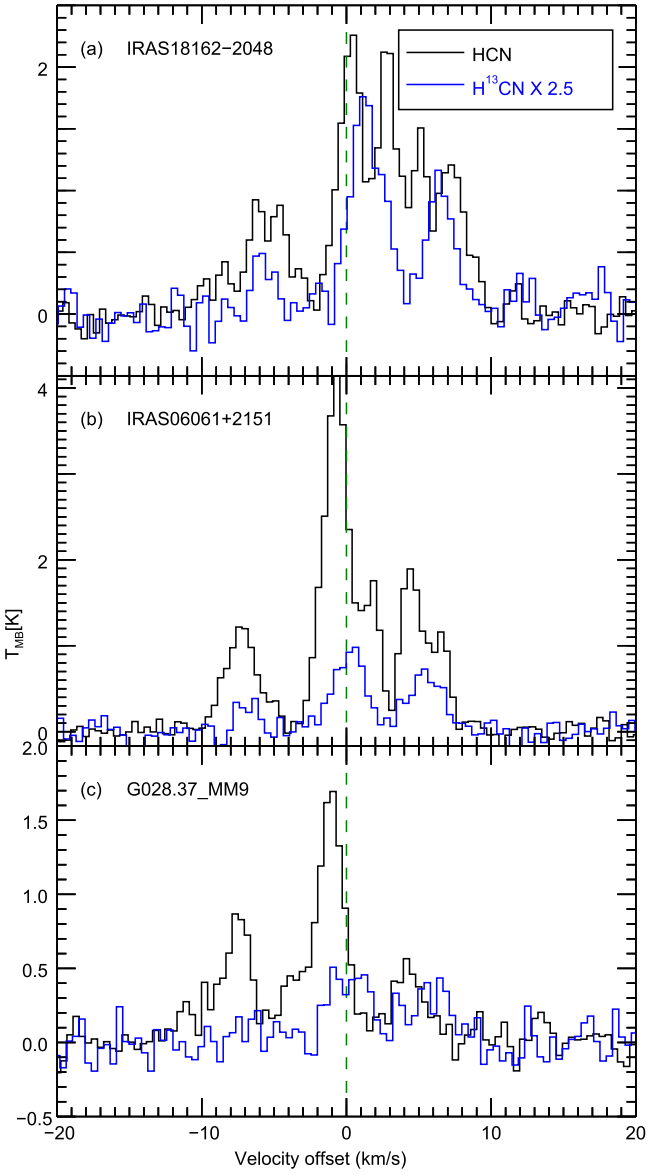

Figure 1. Various features of blue profiles in the HCN $J = 1$–0 line. Both lines are plotted with the velocity relative to the optically thin line's central velocity (green dashed lines).

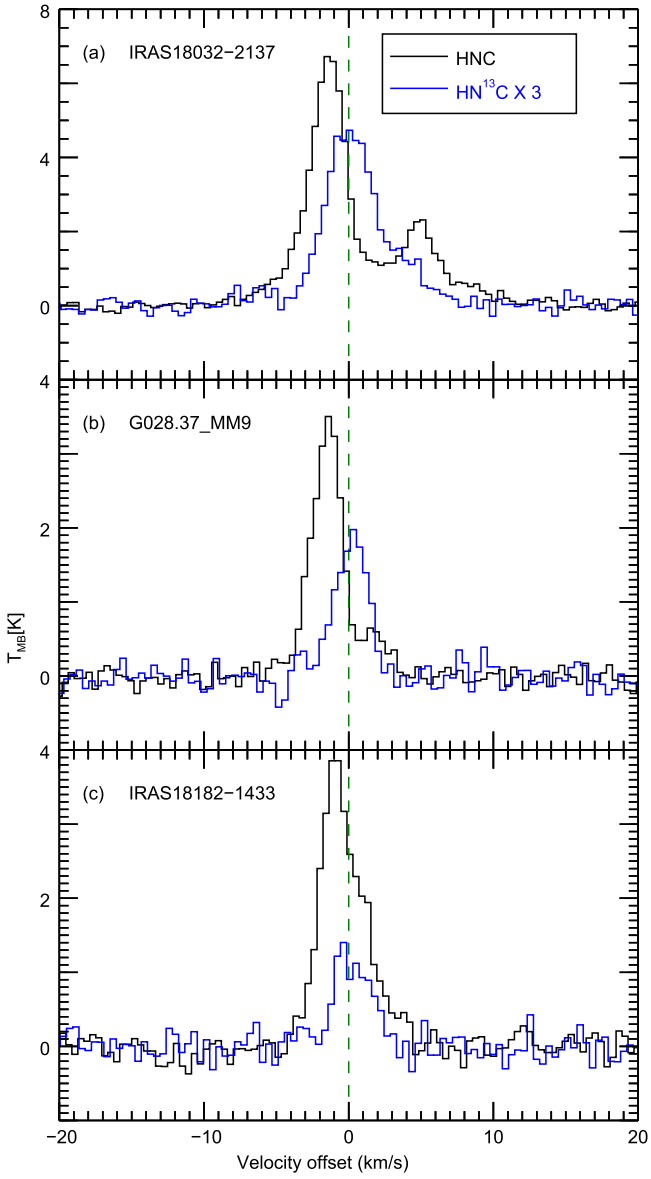

Figure 2. Various features of blue profiles in the HNC $J = 1$–0 line. Both lines are plotted with the velocity relative to the optically thin line's central velocity (green dashed lines).

resulting mean value for each line was less than 0.12 in all the evolutionary stages. For the HCN and $H^{13}CN$ $J = 1$–0 spectra consisting of three apparent hyperfine lines, the strongest hyperfine component ($F = 2$–1) is adopted as a standard for δv calculation. All the line central velocities ($v_{\rm thick}$, $v_{\rm thin}$) and line widths ($\Delta v_{\rm thin}$) are determined from multiple-Gaussian fitting. The HNC $J = 1$–0 line also has a hyperfine structure, but the splitting is too small (~0.7 km s^{-1}; van der Tak et al. 2009) to perform the multiple-Gaussian fitting. As a result, the values of δv were calculated in the same manner, but all the line parameters are measured with a single-Gaussian fitting.

As mentioned above, the strongest hyperfine component ($F = 2$–1) is mainly used for the HCN $J = 1$–0 transition in the δv analysis because this component is detected toward all sources, unlike other weak components, so that we can maximize the sample number for our analysis. Prior to adopting the $F = 2$–1 hyperfine component as standard, we derived the correlations among δv values not only measured from the Gaussian fitting for each HCN hyperfine component, but also measured by fitting the whole hyperfine structure simultaneously. As presented in Figure 3, they show tight correlations in the confidence level above 99%. Therefore, $F = 2$–1 can be representative for all hyperfine components in our analysis. The observed line parameters and derived δv are listed in Tables 3 and 4. Figures 4 and 5 show the distribution of δv derived from the HCN and HNC lines, respectively. The sources located in the left side of the blue dashed line have blue profiles, while those on the right side of the red dashed line have red profiles.

An asymmetric profile may also be induced by another mechanism (e.g., rotation and outflow). If this is the case, a large sample with a random distribution of angles between the axis and the line of sight will not produce an excess of one type of profile (Wu & Evans 2003). So the concept of the "blue excess" was introduced by Mardones et al. (1997) to quantify

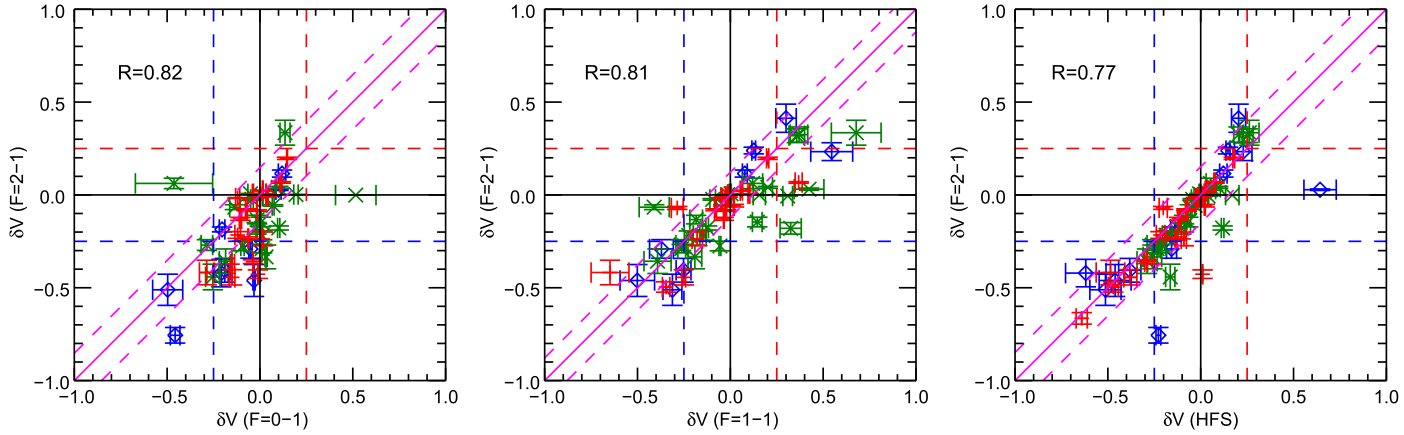

Figure 3. Comparison of the δv values derived from the main hyperfine component ($F = 2$–1) of the HCN $J = 1$–0 line with the values derived from the other hyperfine satellites (left and medium panel) and from the all three hyperfine components at once (right panel). IRDC cores, HMPOs, and UCHIIs are indicated by diamonds, times symbols, and crosses, respectively. The solid line is the line of perfect correlation and the dotted lines indicate 1σ from the line. The Pearson correlation coefficients (R) are given in the upper left corner of each panel, and p-values for all correlations are extremely small. The number of samples in each box is 50, 49, and 61, respectively, from left to right. One HMPO (IRAS 23140+6121) whose value is (δv ($F = 0$–1) $= -1.606$, δv ($F = 2$–1) $= 1.710$) is not presented in the first panel.

the statistics of the line asymmetry in a survey:

$$E = \frac{N_{\rm blue} - N_{\rm red}}{N_{\rm total}} \quad (2)$$

where $N_{\rm blue}$ and $N_{\rm red}$ are the numbers of the blue and red profiles in the total samples ($N_{\rm total}$). These statistical results are summarized in Table 5.

4. DISCUSSION

The values of the blue excess derived from the HCN $J = 1$–0 line for IRDCs, HMPOs, and UCHIIs (0.42, 0.15, and 0.30, respectively) are larger than those derived from the HNC $J = 1$–0 line (0.28, −0.07, and 0.00, respectively). In the HCN spectra, a prevalence of blue profiles relative to red profiles is found in every evolutionary stage, with the IRDCs showing the largest blue excess (Figure 4). In contrast, the distribution of the δv derived from the HNC line is relatively centered on neutral profiles, excepting IRDCs (Figure 5).

We performed a binomial test and calculated the probability P that the one type of excess is induced by chance. The binomial distribution is described as

$$P = \binom{n}{k} p^k (1 - p)^{(n-k)}, \quad (3)$$

where n is the total number of trials, k is the number of successes, and p is the success probability. In this case, n is the total number of sources, k is the number of the blue sources, and the success probability $p = 0.5$ if the distribution shows no bias toward red or blue. Then the possibility that the number of blue sources is equal to or higher than the observed number by chance can be calculated by adding all possibilities $P(n, k, p) + P(n, k+1, p) + \ldots$ until $k = n$. A small value of P indicates that it is unlikely for a blue excess to arise by chance (Rygl et al. 2013). All resulting values of E and P are listed in Table 5. The E of the HCN line is statistically significant with a sufficiently low probability P throughout all evolutionary phases. In the case of the HNC line, in contrast, such a significant value of E appears only in the IRDC phases. The fact that the IRDCs show the highest blue excess in both inflow tracers indicates that the most active inflow occurs in the early phase of massive star formation, even though the characteristics of the blue profile largely depend on the suitable combination of optical depth and critical density. It should be noted that the small sample size of HCN sources in IRDCs would bring about statistical instability in calculating blue excess E. Nevertheless, the probability P as low as 6% indicates that the prevalence of the blue profile is not likely to occur by chance. In addition, the HNC line also shows significant excess to blue in the IRDCs.

4.1. The Astrochemical Effect on the Inflow Tracer

These results suggest that the HCN $J = 1$–0 line is a better inflow tracer than the HNC $J = 1$–0 line in massive star-forming regions. The δv values of the sources detected in both inflow tracers are plotted in Figure 6. The sources located outside the blue/red dashed lines are considered as the blue/red profiles, while the sources located inside those lines are regarded as neutral profiles. Many sources that are blue in HCN are neutral in HNC, but not vice versa, indicating the HNC is less appropriate for tracing inflow motion. We attribute this to an astrochemical effect that reduces the abundance and, hence, the optical depth of HNC.

Jin et al. (2015) have found that the HCN/HNC abundance ratio increases while the optical depth of $HN^{13}C$ decreases as sources evolve from IRDC to UCHIIs, even though both HCN and HNC are mainly formed in equal measure by dissociative recombination (Mendes et al. 2012). One suggested reason for this phenomenon is a neutral–neutral reaction where HNC is selectively consumed at high temperatures ($T_{\rm K} \geqslant 24$ K; Hirota et al. 1998). Hirota et al. (1998) showed that the HCN abundances in the high kinetic temperature regions (OMC-1 cores) are comparable to those in the dark cloud cores, whereas the HNC abundances decrease as the temperature increases. By this astrochemical effect, the opacity of the HNC line would decrease as an object evolves, so that the line cannot trace inflow motion well; an inflow profile appears in lines that are sufficiently opaque (Myers et al. 1996). In Figure 6, a significant number of HMPO and UCHII sources are bluer in HCN than HNC. In contrast, the HNC line is rather bluer in the IRDCs, and this opposite tendency is more obvious in qIRDCc

Table 3
Derived HCN Line Parameters

Classification	Source Name	$v_{\rm thick}$ (km s^{-1})	$v_{\rm thin}$ (km s^{-1})	$\Delta v_{\rm thin}$ (km s^{-1})	δv	Profile(δv)
qIRDCc	G028.37_MM9	78.37 (0.041)	79.69 (0.217)	3.25 (0.509)	−0.41 (0.102)	Blue
	G035.39_MM5	43.83 (0.054)	45.01 (0.156)	2.30 (0.377)	−0.51 (0.124)	Blue
aIRDCc	G022.35_MM1[a]	44.85 (0.190)	44.55 (0.162)	2.97 (0.404)	0.10 (0.119)	Neutral
	G030.97_MM1	78.30 (0.035)	77.85 (0.068)	1.91 (0.146)	0.24 (0.057)	Neutral
	G031.97_MM1	93.92 (0.211)	94.63 (0.079)	3.81 (0.272)	−0.19 (0.077)	Neutral
	G033.69_MM4	104.46 (0.103)	106.00 (0.240)	3.66 (0.644)	−0.42 (0.120)	Blue
	G033.69_MM5	105.49 (0.087)	105.13 (0.106)	1.57 (0.324)	0.23 (0.132)	Neutral
	G034.43_MM4	54.86 (0.057)	57.47 (0.066)	3.46 (0.194)	−0.76 (0.055)	Blue
	G035.39_MM7	45.02 (0.109)	45.56 (0.150)	1.83 (0.315)	−0.29 (0.150)	Blue
	G048.65_MM1	33.82 (0.046)	34.22 (0.076)	0.87 (0.161)	−0.46 (0.165)	Blue
	G053.25_MM4	24.57 (0.030)	24.12 (0.097)	1.09 (0.202)	0.41 (0.139)	Red
	G053.25_MM6	23.45 (0.042)	23.31 (0.119)	1.26 (0.209)	0.11 (0.129)	Neutral
HMPO	IRAS 00117+6412	−35.97 (0.079)	−36.03 (0.111)	0.92 (0.412)	0.06 (0.209)	Neutral
	IRAS 05358+3543	−17.84 (0.025)	−17.31 (0.070)	1.95 (0.183)	−0.28 (0.055)	Blue
	IRAS 05373+2349	2.09 (0.030)	2.29 (0.083)	1.56 (0.288)	−0.13 (0.076)	Neutral
	IRAS 18151-1208	33.02 (0.014)	33.61 (0.100)	2.20 (0.236)	−0.27 (0.059)	Blue
	IRAS 18182-1433	58.30 (0.211)	59.28 (0.116)	3.38 (0.270)	−0.29 (0.099)	Blue
	IRAS 18223-1243	44.67 (0.021)	45.29 (0.079)	1.40 (0.217)	−0.44 (0.099)	Blue
	IRAS 18264-1152	43.28 (0.034)	43.75 (0.054)	2.63 (0.158)	−0.18 (0.035)	Neutral
	IRAS 18308-0841	77.72 (0.050)	76.81 (0.128)	2.87 (0.332)	0.32 (0.072)	Red
	IRAS 18440-0148	97.53 (0.066)	98.03 (0.160)	2.29 (0.259)	−0.22 (0.102)	Neutral
	IRAS 18445-0222	86.96 (0.045)	86.94 (0.259)	2.46 (0.672)	0.01 (0.123)	Neutral
	IRAS 18447-0229	102.43 (0.133)	102.43 (0.134)	1.37 (0.291)	−0.00 (0.194)	Neutral
	IRAS 18470-0044	97.27 (0.100)	96.30 (0.135)	2.99 (0.379)	0.32 (0.089)	Red
	IRAS 18527+0301	74.94 (0.075)	75.75 (0.179)	2.42 (0.465)	−0.33 (0.123)	Blue
	IRAS 18530+0215	77.07 (0.022)	77.08 (0.087)	2.78 (0.233)	−0.01 (0.039)	Neutral
	IRAS 19012+0536	64.84 (0.111)	65.58 (0.151)	2.08 (0.385)	−0.36 (0.142)	Blue
	IRAS 19035+0641	32.41 (0.078)	32.33 (0.184)	2.64 (0.502)	0.03 (0.099)	Neutral
	IRAS 19410+2336	22.13 (0.016)	22.70 (0.116)	2.66 (0.287)	−0.22 (0.055)	Neutral
	IRAS 19411+2306	29.31 (0.026)	29.34 (0.109)	1.62 (0.248)	−0.02 (0.084)	Neutral
	IRAS 19413+2332	20.03 (0.024)	20.29 (0.132)	1.47 (0.256)	−0.18 (0.111)	Neutral
	IRAS 20126+4104	−3.80 (0.025)	−3.65 (0.070)	2.55 (0.194)	−0.06 (0.037)	Neutral
	IRAS 20216+4107	−1.65 (0.032)	−1.59 (0.094)	1.03 (0.218)	−0.07 (0.123)	Neutral
	IRAS 20343+4129	11.48 (0.016)	11.48 (0.109)	2.38 (0.230)	0.00 (0.052)	Neutral
	IRAS 22134+5834	−17.82 (0.076)	−18.39 (0.106)	1.69 (0.337)	0.33 (0.127)	Red
	IRAS 22198+6336	−11.24 (0.029)	−11.05 (0.083)	1.32 (0.238)	−0.15 (0.089)	Neutral
	IRAS 23033+5951	−53.18 (0.033)	−53.28 (0.143)	2.52 (0.318)	0.04 (0.070)	Neutral
	IRAS 23140+6121	−53.18 (0.033)	−50.74 (0.244)	1.43 (0.496)	−1.71 (0.626)	Blue
UCHII	IRAS 02232+6138	−47.78 (0.024)	−46.55 (0.035)	3.43 (0.092)	−0.36 (0.020)	Blue
	IRAS 02575+6017	−38.13 (0.018)	−37.94 (0.060)	2.35 (0.150)	−0.08 (0.034)	Neutral
	IRAS 03035+5819	−39.60 (0.024)	−39.57 (0.061)	1.69 (0.160)	−0.02 (0.050)	Neutral
	IRAS 06053-0622	9.53 (0.029)	10.07 (0.084)	1.29 (0.204)	−0.42 (0.110)	Blue
	IRAS 06056+2131	2.55 (0.007)	2.74 (0.057)	2.28 (0.137)	−0.08 (0.029)	Neutral
	IRAS 06058+2138	3.36 (0.008)	3.35 (0.053)	2.69 (0.126)	0.01 (0.023)	Neutral
	IRAS 06061+2151	−1.26 (0.015)	−0.30 (0.084)	2.58 (0.203)	−0.37 (0.048)	Blue
	IRAS 06084-0611	11.65 (0.014)	11.09 (0.034)	2.88 (0.090)	0.20 (0.018)	Neutral
	IRAS 06099+1800	7.33 (0.007)	7.35 (0.031)	2.30 (0.083)	−0.01 (0.017)	Neutral
	IRAS 17599-2148	20.24 (0.023)	20.61 (0.265)	6.31 (0.746)	−0.06 (0.046)	Neutral
	IRAS 18075-1956	−3.99 (0.113)	−2.95 (0.244)	4.81 (0.627)	−0.22 (0.079)	Neutral
	IRAS 18162-2048	11.22 (0.043)	12.40 (0.062)	2.77 (0.154)	−0.43 (0.045)	Blue
	IRAS 18174-1612	19.66 (0.014)	19.45 (0.059)	3.09 (0.162)	0.07 (0.024)	Neutral
	IRAS 18317-0757	78.41 (0.050)	79.86 (0.067)	2.91 (0.167)	−0.50 (0.049)	Blue
	IRAS 18434-0242	96.52 (0.027)	97.38 (0.051)	3.66 (0.137)	−0.23 (0.023)	Neutral
	IRAS 18469-0132	87.37 (0.024)	88.09 (0.187)	3.04 (0.474)	−0.24 (0.079)	Neutral
	IRAS 20255+3712	−1.52 (0.020)	−1.37 (0.084)	2.09 (0.255)	−0.07 (0.051)	Neutral
	IRAS 20178+4046	1.03 (0.016)	1.03 (0.071)	1.64 (0.152)	0.00 (0.053)	Neutral
	IRAS 20350+4126	−3.88 (0.035)	−2.85 (0.089)	2.33 (0.229)	−0.44 (0.069)	Blue
	IRAS 22176+6303	−6.80 (0.007)	−6.77 (0.030)	2.63 (0.071)	−0.01 (0.014)	Neutral
	IRAS 22543+6145	−12.41 (0.018)	−10.40 (0.056)	3.01 (0.144)	−0.67 (0.040)	Blue
	IRAS 23133+6050	−56.48 (0.020)	−56.16 (0.055)	2.49 (0.148)	−0.13 (0.031)	Neutral
	IRAS 23138+5945	−44.56 (0.055)	−44.64 (0.145)	3.33 (0.339)	0.02 (0.060)	Neutral

Note.
[a] The $F = 0$–1 hyperfine component is adopted as a standard for δv calculation.

Table 4
Derived HNC Line Parameters

Classification	Source Name	$v_{\rm thick}$ (km s^{-1})	$v_{\rm thin}$ (km s^{-1})	$\Delta v_{\rm thin}$ (km s^{-1})	δv	Profile(δv)	$\frac{T(B)}{T(R)}$	Profile $\left(\frac{T(B)}{T(R)}\right)$	$v_{\rm dip}$ (km s^{-1})
qIRDCc	G028.37_MM9	78.48 (0.028)	80.16 (0.062)	2.63 (0.144)	−0.64 (0.049)	Blue	5.66	Blue	80.82
	G031.97_MM9	96.06 (0.051)	96.75 (0.202)	5.39 (0.456)	−0.13 (0.048)	Neutral	1.21	Neutral	97.27
	G035.39_MM5	44.12 (0.029)	45.51 (0.059)	1.64 (0.165)	−0.85 (0.101)	Blue	⋯	⋯	⋯
aIRDCc	G015.31_MM3	31.27 (0.105)	31.04 (0.057)	0.99 (0.116)	0.23 (0.166)	Neutral	⋯	⋯	⋯
	G023.60_MM1	106.75 (0.044)	106.74 (0.137)	4.35 (0.319)	0.00 (0.042)	Neutral	0.94	Neutral	106.25
	G023.60_MM6	53.10 (0.040)	53.23 (0.081)	1.77 (0.182)	−0.08 (0.069)	Neutral	⋯	⋯	⋯
	G024.60_MM1	54.11 (0.035)	53.11 (0.091)	1.88 (0.196)	0.53 (0.087)	Red	⋯	⋯	⋯
	G028.37_MM4	78.50 (0.023)	79.31 (0.066)	3.17 (0.157)	−0.41 (0.035)	Blue	⋯	⋯	⋯
	G028.37_MM6	78.32 (0.054)	80.29 (0.043)	2.37 (0.105)	−0.83 (0.055)	Blue	3.26	Blue	81.44
	G030.97_MM1	77.95 (0.018)	77.95 (0.075)	2.47 (0.197)	−0.00 (0.038)	Neutral	⋯	⋯	⋯
	G031.97_MM1	94.34 (0.026)	95.42 (0.058)	3.51 (0.140)	−0.31 (0.027)	Blue	⋯	⋯	⋯
	G031.97_MM8	94.25 (0.065)	94.70 (0.079)	2.46 (0.245)	−0.18 (0.061)	Neutral	2.62	Blue	97.89
	G033.69_MM4	105.78 (0.048)	106.11 (0.071)	3.35 (0.180)	−0.10 (0.036)	Neutral	⋯	⋯	⋯
	G033.69_MM5	105.20 (0.035)	105.25 (0.073)	1.97 (0.193)	−0.02 (0.055)	Neutral	⋯	⋯	⋯
	G034.43_MM1	58.14 (0.024)	57.79 (0.052)	2.85 (0.116)	0.12 (0.027)	Neutral	0.56	Red	57.26
	G034.43_MM3	59.48 (0.029)	59.41 (0.039)	2.15 (0.103)	0.03 (0.032)	Neutral	⋯	⋯	⋯
	G034.43_MM4	56.75 (0.035)	57.76 (0.039)	2.47 (0.098)	−0.41 (0.034)	Blue	⋯	⋯	⋯
	G035.59_MM3	44.40 (0.036)	44.76 (0.065)	1.34 (0.137)	−0.27 (0.080)	Blue	⋯	⋯	⋯
	G038.95_MM3	42.58 (0.040)	42.27 (0.094)	2.20 (0.249)	0.14 (0.063)	Neutral	⋯	⋯	⋯
	G038.95_MM4	42.03 (0.040)	42.30 (0.107)	1.40 (0.307)	−0.19 (0.113)	Neutral	⋯	⋯	⋯
	G048.65_MM1	33.78 (0.030)	34.03 (0.120)	1.65 (0.257)	−0.15 (0.094)	Neutral	⋯	⋯	⋯
	G048.65_MM2	33.62 (0.032)	33.85 (0.106)	1.07 (0.209)	−0.22 (0.136)	Neutral	⋯	⋯	⋯
	G053.25_MM4	24.48 (0.012)	24.43 (0.040)	1.19 (0.094)	0.04 (0.044)	Neutral	⋯	⋯	⋯
	G053.25_MM6	23.55 (0.019)	23.74 (0.089)	1.45 (0.178)	−0.13 (0.077)	Neutral	⋯	⋯	⋯
	G053.31_MM2	25.03 (0.029)	25.57 (0.086)	1.31 (0.216)	−0.41 (0.111)	Blue	⋯	⋯	⋯
HMPO	IRAS 05358+3543	−17.64 (0.013)	−17.40 (0.076)	1.74 (0.201)	−0.14 (0.054)	Neutral	⋯	⋯	⋯
	IRAS 05373+2349	2.26 (0.016)	2.42 (0.072)	1.57 (0.218)	−0.10 (0.058)	Neutral	⋯	⋯	⋯
	IRAS 18024-2119	0.93 (0.117)	0.60 (0.063)	2.11 (0.153)	0.15 (0.086)	Neutral	⋯	⋯	⋯
	IRAS 18089-1732	34.34 (0.069)	32.78 (0.080)	3.39 (0.170)	0.46 (0.050)	Red	0.47	Red	33.36
	IRAS 18102-1800	21.67 (0.058)	21.41 (0.086)	2.07 (0.196)	0.13 (0.071)	Neutral	⋯	⋯	⋯
	IRAS 18144-1723	47.86 (0.040)	47.61 (0.076)	3.29 (0.180)	0.08 (0.035)	Neutral	0.77	Red	47.78
	IRAS 18151-1208	33.10 (0.020)	33.37 (0.073)	1.89 (0.180)	−0.14 (0.051)	Neutral	⋯	⋯	⋯
	IRAS 18162-1612	61.86 (0.028)	61.86 (0.092)	1.77 (0.228)	−0.00 (0.068)	Neutral	⋯	⋯	⋯
	IRAS 18182-1433	58.85 (0.031)	59.66 (0.112)	3.04 (0.258)	−0.26 (0.052)	Blue	⋯	⋯	⋯
	IRAS 18223-1243	45.33 (0.025)	45.29 (0.067)	1.85 (0.156)	0.03 (0.050)	Neutral	⋯	⋯	⋯
	IRAS 18264-1152	43.99 (0.017)	43.83 (0.076)	2.41 (0.183)	0.07 (0.039)	Neutral	⋯	⋯	⋯
	IRAS 18290-0924	84.29 (0.064)	84.47 (0.111)	1.98 (0.267)	−0.09 (0.089)	Neutral	⋯	⋯	⋯
	IRAS 18310-0825	84.46 (0.076)	84.67 (0.089)	1.83 (0.222)	−0.12 (0.091)	Neutral	⋯	⋯	⋯
	IRAS 18345-0641	95.46 (0.082)	95.48 (0.063)	1.79 (0.152)	−0.01 (0.081)	Neutral	⋯	⋯	⋯
	IRAS 18440-0148	97.69 (0.029)	97.67 (0.153)	1.47 (0.433)	0.02 (0.124)	Neutral	⋯	⋯	⋯
	IRAS 18470-0044	96.49 (0.067)	96.31 (0.162)	2.52 (0.462)	0.07 (0.092)	Neutral	0.59	Red	95.71
	IRAS 18488+0000	82.78 (0.141)	83.36 (0.182)	2.95 (0.439)	−0.20 (0.113)	Neutral	⋯	⋯	⋯
	IRAS 18511+0146	57.10 (0.038)	56.94 (0.061)	1.77 (0.145)	0.09 (0.056)	Neutral	⋯	⋯	⋯
	IRAS 18530+0215	77.25 (0.016)	77.30 (0.100)	2.73 (0.219)	−0.02 (0.042)	Neutral	⋯	⋯	⋯
	IRAS 19220+1432	69.27 (0.104)	69.78 (0.298)	3.11 (0.516)	−0.16 (0.132)	Neutral	⋯	⋯	⋯
	IRAS 19411+2306	29.35 (0.019)	29.24 (0.088)	1.60 (0.233)	0.12 (0.110)	Neutral	⋯	⋯	⋯
	IRAS 20126+4104	−3.45 (0.015)	−3.95 (0.048)	1.95 (0.110)	0.26 (0.035)	Red	⋯	⋯	⋯
	IRAS 20216+4107	−1.57 (0.025)	−1.63 (0.054)	0.97 (0.118)	0.06 (0.082)	Neutral	⋯	⋯	⋯
	IRAS 20293+3952	6.06 (0.026)	5.96 (0.117)	2.32 (0.281)	0.04 (0.062)	Neutral	⋯	⋯	⋯
	IRAS 20343+4129	11.15 (0.022)	11.73 (0.123)	2.29 (0.261)	−0.25 (0.070)	Blue	⋯	⋯	⋯
	IRAS 22134+5834	−18.24 (0.064)	−18.80 (0.142)	1.54 (0.260)	0.37 (0.147)	Red	0.94	Neutral	-18.40
	IRAS 22198+6336	−11.12 (0.061)	−10.97 (0.065)	1.25 (0.164)	−0.12 (0.102)	Neutral	⋯	⋯	⋯
	IRAS 23033+5951	−52.79 (0.034)	−53.69 (0.185)	3.13 (0.450)	0.29 (0.081)	Red	⋯	⋯	⋯
UCHII	IRAS 02232+6138	−46.88 (0.033)	−46.35 (0.077)	2.90 (0.178)	−0.18 (0.040)	Neutral	⋯	⋯	⋯
	IRAS 02575+6017	−38.24 (0.019)	−37.97 (0.067)	1.37 (0.145)	−0.20 (0.066)	Neutral	⋯	⋯	⋯
	IRAS 05393-0156	10.34 (0.046)	9.47 (0.074)	0.57 (0.148)	1.52 (0.447)	Red	1.09	Neutral	10.57
	IRAS 06056+2131	2.67 (0.010)	2.83 (0.107)	2.58 (0.277)	−0.06 (0.046)	Neutral	⋯	⋯	⋯
	IRAS 06058+2138	3.31 (0.010)	3.40 (0.075)	2.00 (0.182)	−0.04 (0.043)	Neutral	⋯	⋯	⋯
	IRAS 06084-0611	11.69 (0.020)	11.31 (0.077)	2.25 (0.185)	0.17 (0.045)	Neutral	⋯	⋯	⋯
	IRAS 06099+1800	7.32 (0.010)	7.32 (0.082)	1.79 (0.205)	−0.00 (0.052)	Neutral	⋯	⋯	⋯
	IRAS 17574-2403	9.01 (0.017)	8.95 (0.032)	3.78 (0.087)	0.02 (0.013)	Neutral	⋯	⋯	⋯
	IRAS 17599-2148	20.10 (0.031)	18.87 (0.106)	4.15 (0.241)	0.30 (0.037)	Red	0.38	Red	18.00
	IRAS 18032-2137	33.50 (0.047)	35.10 (0.041)	4.48 (0.110)	−0.36 (0.021)	Blue	3.32	Blue	37.74

Table 4
(Continued)

Classification	Source Name	$v_{\rm thick}$ (km s^{-1})	$v_{\rm thin}$ (km s^{-1})	$\Delta v_{\rm thin}$ (km s^{-1})	δv	Profile(δv)	$\frac{T(B)}{T(R)}$	Profile $\left(\frac{T(B)}{T(R)}\right)$	$v_{\rm dip}$ (km s^{-1})
	IRAS 18075-1956	−3.13 (0.029)	−2.00 (0.193)	2.75 (0.472)	−0.41 (0.107)	Blue	⋯	⋯	⋯
	IRAS 18162-2048	12.36 (0.024)	12.46 (0.130)	2.37 (0.262)	−0.04 (0.065)	Neutral	1.30	Blue	12.51
	IRAS 18100-1854	39.96 (0.037)	38.37 (0.051)	3.95 (0.112)	0.40 (0.025)	Red	0.41	Red	36.99
	IRAS 18403-0417	96.26 (0.053)	95.74 (0.071)	4.44 (0.186)	0.12 (0.028)	Neutral	1.62	Blue	97.56
	IRAS 18434-0242	96.85 (0.015)	97.56 (0.055)	3.02 (0.137)	−0.24 (0.026)	Neutral	⋯	⋯	⋯
	IRAS 19095+0930	44.12 (0.062)	44.12 (0.247)	4.77 (0.610)	0.00 (0.065)	Neutral	⋯	⋯	⋯
	IRAS 20081+3122	12.52 (0.022)	11.74 (0.068)	3.91 (0.168)	0.20 (0.025)	Neutral	⋯	⋯	⋯
	IRAS 20255+3712	−1.41 (0.019)	−1.49 (0.074)	1.92 (0.215)	0.04 (0.049)	Neutral	⋯	⋯	⋯
	IRAS 20178+4046	0.98 (0.012)	1.07 (0.097)	1.87 (0.216)	−0.05 (0.058)	Neutral	⋯	⋯	⋯
	IRAS 20350+4126	−3.01 (0.035)	−2.46 (0.110)	2.27 (0.282)	−0.24 (0.071)	Neutral	⋯	⋯	⋯
	IRAS 22176+6303	−6.84 (0.008)	−6.83 (0.082)	2.27 (0.184)	−0.01 (0.040)	Neutral	⋯	⋯	⋯
	IRAS 22543+6145	−11.38 (0.024)	−10.61 (0.117)	2.80 (0.268)	−0.27 (0.057)	Blue	1.78	Blue	−10.12
	IRAS 23138+5945	−44.49 (0.031)	−44.44 (0.155)	2.12 (0.381)	−0.03 (0.088)	Neutral	⋯	⋯	⋯

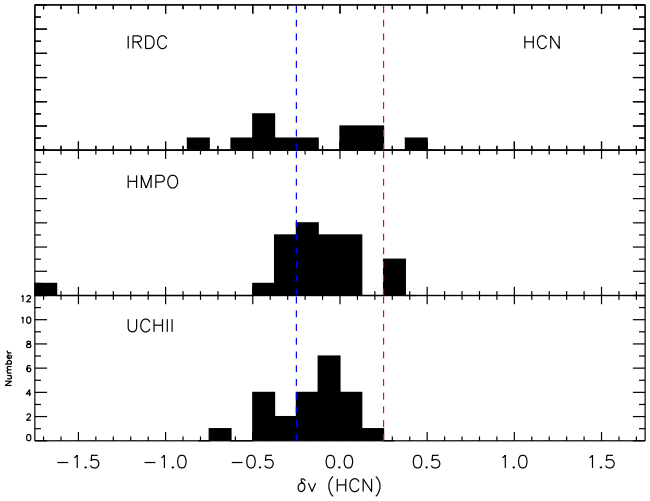

Figure 4. Distribution of δv values calculated from the HCN $J = 1$–0 line. The sources located outside the blue/red dashed lines can be considered as blue/red profiles, whereas the sources inside the blue and red dashed lines are neutral profiles. The top, middle, and bottom panels present results from 12 IRDC cores, 26 HMPOs, and 23 UCHIIs, respectively.

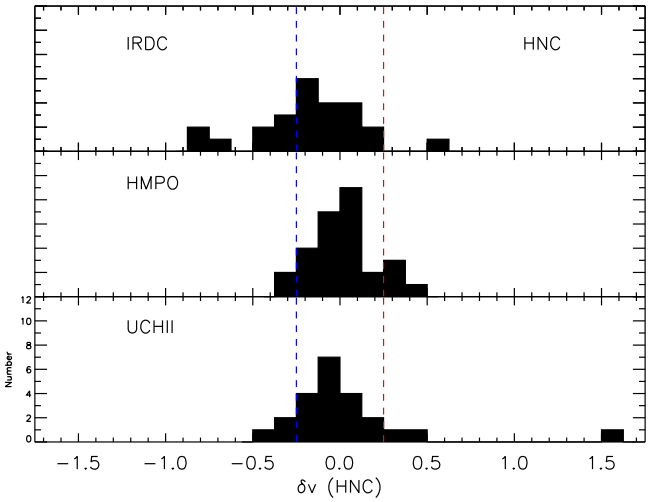

Figure 5. Distribution of δv values calculated from the HNC $J = 1$–0 line. The sources located outside the blue/red dashed lines can be considered as blue/red profiles, whereas the sources inside the blue and red dashed lines are neutral profiles. The top, middle, and bottom panels represent results from 25 IRDC cores, 28 HMPOs, and 23 UCHIIs, respectively.

Table 5
Blue Excess (E) Statistics

Evolutionary Stage	Inflow Tracer	$N_{\rm Blue}$	$N_{\rm Red}$	$N_{\rm Total}$	E	P
IRDCs	HCN	6	1	12	0.42	0.062
	HNC	8	1	25	0.28	0.019
HMPOs	HCN	7	3	26	0.15	0.172
	HNC	2	4	28	−0.07	0.891
UCHIIs	HCN	7	0	23	0.30	0.008
	HNC	3	3	23	0.00	0.500

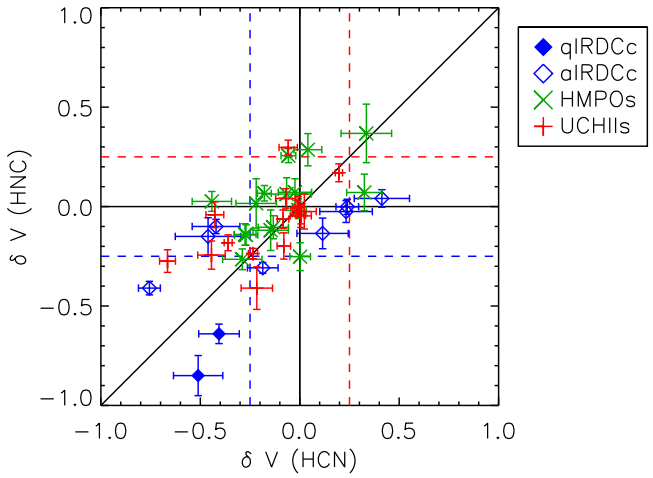

Figure 6. Comparison of δv values between HNC and HCN. Only the sources where we can analyze both inflow tracers are plotted here. IRDC cores, HMPOs, and UCHIIs are indicated by diamonds, times symbols, and crosses, respectively. Here IRDC cores are divided into quiescent cores (qIRDCc, filled diamonds) and active cores (aIRDCc, open diamonds), depending on star-forming activity. The sources located outside the blue/red dashed lines can be considered as blue/red profiles. One UCHII source whose value is (−0.137, 1.524) is not presented here.

than aIRDCc, supporting our scenario again. The qIRDCc is considered to be in the earlier phase (Chambers et al. 2009) and shows a smaller value for the HCN/HNC abundance ratio than aIRDCc (Jin et al. 2015). This result highlights the importance of considering chemistry when studying the dynamics of star-forming regions.

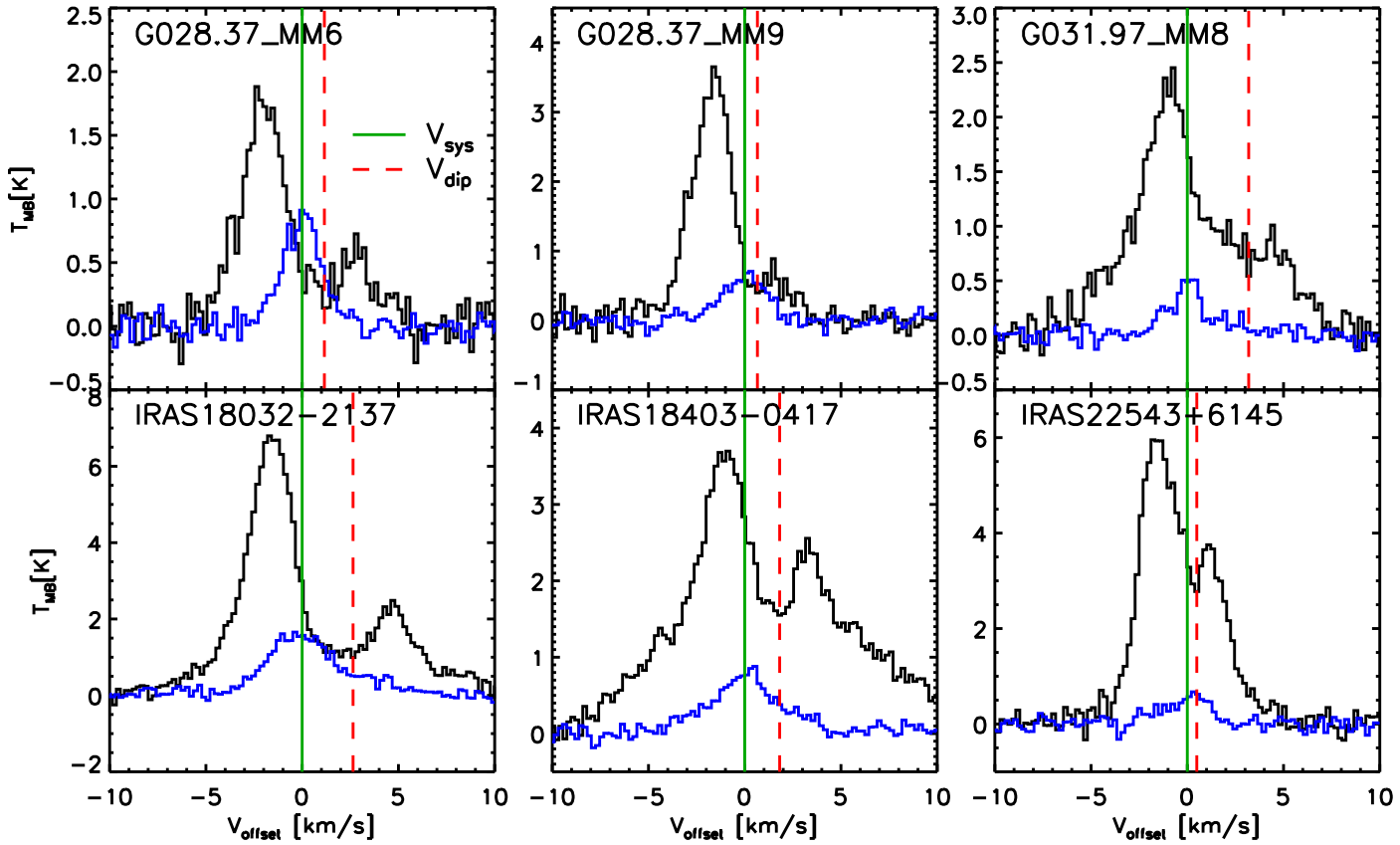

Figure 7. The blue profile with a redshifted absorption dip in the HNC $J = 1$–0 line. Both HNC (black) and $HN^{13}C$ (blue) lines are plotted with the velocity relative to the systemic velocity (green solid lines). The red dashed line represents the dip position.

4.2. Comparison to Previous Studies

There have been many attempts to examine the inflow signature, as mentioned in Section 1. Some of those studies have suggested the HCO^+ $J = 1$–0 line as the best inflow tracer in massive star-forming regions. We compare our results not only with the previous inflow surveys using the HCO^+ $J = 1$–0 line, but also with the study using a higher transition line of HCN.

In the HCO^+ $J = 1$–0 line, IRDCs seem to undergo the most detectable active inflow process (Purcell et al. 2006; Rygl et al. 2013; He et al. 2015), whereas sources in more evolved phases such as HMPOs and UCHIIs show less inflow, as indicated by smaller values of the blue excess. For example, Purcell et al. (2006) reported a blue excess as low as 0.02 toward these evolved samples, and He et al. (2015) found a decreasing tendency of the blue excess with evolution from IRDCs to UCHIIs. The blue excesses that we observed with the HCN $J = 1$–0 lines are comparable to their values for each evolutionary stage, with the largest value in IRDCs. This indicates that the HCN $J = 1$–0 line is as sensitive as the HCO^+ $J = 1$–0 line in high-mass star-forming regions.

For a higher transition of HCN, Wu & Evans (2003) surveyed inflow motion using the HCN $J = 3$–2 line. They reported a blue excess of 0.21 in the sources consisting of the 28 H II regions where star-forming activity still appears. This value is much smaller than the blue excess for our UCHII sample (0.30 for 23 UCHIIs), showing that the 1–0 transition line of HCN traces the inflow motion better than the higher transition line. This result is consistent with the results of Fuller et al. (2005): the lower transition lines of HCO^+ show the most inflow signature. They observed the HCO^+ $J = 1$–0, 3–2, and 4–3 transitions toward HMPOs and found the highest blue excess in the $J = 1$–0 line. This result may be related to the gas motion (i.e., velocity profile) that the high energy level transitions trace; the higher transition lines emit from the hotter and denser central region. According to the model of a collapsing cloud in massive star-forming regions, the velocity gradient at the central region is too large to make the self-absorption feature in high energy transitions (Smith et al. 2013).

4.3. Global Collapse?

An interesting feature in the double-peaked HNC spectra is that the absorption dips in six out of seven blue sources are redshifted relative to the systemic velocities. For the sources whose lines are strongly self-absorbed, the asymmetries of the spectra are determined using the $T(B)/T(R)$ parameter. The fluxes of the two peaks are measured by the double-Gaussian fitting, and if the differences between the peaks are larger than the 3σ noise level, we classify them into blue/red profiles, otherwise they are classified as neutral profiles. Some sources that are suspected to have a wing-like structure, however, could not be fitted by the double-Gaussians directly, even though an obvious self-absorption feature appears. Those lines are fitted after masking the wing-like structures. After that, we compare the velocity of the absorption dip ($v_{\rm dip}$) with the systemic velocity determined from the $HN^{13}C$ line. The $v_{\rm dip}$ is identified as the velocity at the lowest flux in the absorption dip by cursor. If the velocity deviation of the absorption dip exceeds three times the measurement error of the systemic velocity, the line is considered to have a shifted dip. The asymmetry parameters ($T(B)/T(R)$), the velocities of the absorption

dips (v_{dip}) of the HNC $J = 1–0$ line, and the central velocities of the $HN^{13}C$ $J = 1–0$ line (v_{thin}) are listed in Table 4. We also tried to perform the same analysis in the HCN spectra. However, the double-Gaussian fitting was not reliable because of the combination of the line blending effects among the hyperfine components and the self-absorption.

According to the above analysis, six out of seven blue sources have absorption dips redshifted relative to their systemic velocity (Figure 7). If considering a turbulent core accretion model, the star formation occurs in quasi-equilibrium molecular cloud where inflow occurs in localized regions. This would make the absorption dip at the source velocity. However, if the cloud clumps form in global collapse, as described in the competitive accretion model, even the outer larger region takes part in the inflowing process, making the absorption dip redshifted. Therefore, these redshifted absorption dips detected in our sources may indicate global collapse candidates. Actually, Smith et al. (2013) calculated the line profiles of HCO^+ in a core following the competitive accretion formalism and frequently found a non-central self-absorption dip. However, depending on the optical depth, a redshifted absorption dip can be also induced by the absorption in the inner collapsing regions. Mapping observations with better resolution are needed to rule out this possibility.

5. SUMMARY

To understand the gravitational inflow taking place in high-mass star formation, we surveyed 54 IRDC cores, 69 HMPOs, and 54 UCHIIs in the HCN $J = 1–0$ and HNC $J = 1–0$ lines.

1. We found a statistically significant blue excess of the HCN line for every evolutionary phase (0.42, 0.15, and 0.30 for IRDCs, HMPOs, and UCHIIs, respectively). These are comparable to the values derived using other inflow tracers, including HCO^+ $J = 1–0$, known to be one of the best inflow tracers. This indicates the HCN line is a good tracer of gravitational inflow.
2. With the HNC line, the blue profile appears significant only in IRDCs. We conclude that this line is not appropriate to trace inflow motion in the evolved stages of massive star formation because the HNC abundance (and thus, its optical depth) decreases at high temperatures. This result highlights the importance of considering chemistry when studying the dynamics of massive star-forming regions.
3. The fact that IRDCs show the highest blue excess in both inflow tracers indicates that the IRDC phase is undergoing the most active inflow process. This result is consistent with the general prediction for the inflow process, where younger sources are expected to be more actively inflowing onto the central source. However, it is also likely that inflowing still matters for UCHIIs.
4. We found that the absorption dips of the HNC $J = 1–0$ spectra are redshifted relative to the systemic velocities in six out of seven blue sources. These redshifted absorption dips suggest that the clumps are in global collapse. Mapping observations with better angular resolutions are needed to examine this feature in more detail.

We are grateful to all the staff members at KVN who helped to operate the telescope. The KVN is a facility operated by the Korea Astronomy and Space Science Institute. This work was supported by the Basic Science Research Program through the National Research Foundation of Korea (NRF) (grant No. NRF-2015R1A2A2A01004769) and the Korea Astronomy and Space Science Institute under the R & D program (Project No. 2015-1-320-18) supervised by the Ministry of Science, ICT, and Future Planning.

REFERENCES

Beuther, H., & Schilke, P. 2004, Sci, 303, 1167
Beuther, H., Schilke, P., Menten, K. M., et al. 2002, ApJS, 566, 945
Bhattacharya, B. N., & Gordy, W. 1960, PhRv, 119, 144
Blackman, G. L., Brown, R. D., Godfrey, P. D., & Gunn, H. I. 1976, Natur, 261, 395
Bodenheimer, P. H. 2011, Principles of Star Formation (Berlin: Springer-Verlag)
Bonnell, I. A., Bate, M. R., Clarke, C. J., & Pringle, J. E. 2001, MNRAS, 323, 785
Chambers, E. T., Jackson, J. M., Rathborne, J. M., & Simon, R. 2009, ApJS, 181, 360
Di Francesco, J., Johnstone, D., Kirk, H. M., MacKenzie, T., & Ledwosinska, E. 2008, ApJS, 175, 277
Egan, M. P., Shimpman, R. F., Price, S. D., Carey, S. J., & Clark, F. O. 1998, ApJL, 494, L199
Fuller, G. A., Williams, S. J., & Sridharan, T. K. 2005, A&A, 442, 949
He, Y.-X., Zhou, J.-J., Esimbek, J., et al. 2015, MNRAS, 450, 1926
Hirota, T., Yamamoto, S., Mikami, H., et al. 1998, ApJ, 503, 717
Jin, M., Lee, J.-E., & Kim, K.-T. 2015, ApJS, 219, 2
Kim, K.-T., Byun, D.-Y., Je, D.-H., et al. 2011, JKAS, 44, 81
Kim, K.-T., & Koo, B.-C. 2001, ApJ, 549, 979
Klaassen, P. D., Testi, L., & Beuther, H. 2012, A&A, 538, A140
Krumholz, M. R., & Bonnell, I. A. 2009, in Structure Formation in Astrophysics, ed. G. Chabrier (Cambridge: Cambridge Univ. Press), 288
Krumholz, M. R., & Tan, J. C. 2007, ApJ, 654, 304
Kurtz, S., Churchwell, E., & Wood, D. O. S. 1994, ApJS, 91, 659
Lee, S.-S., Byun, D.-Y., Oh, C. S., et al. 2011, PASP, 123, 1398
Mardones, D., Myers, P. C., Tafalla, M., & Wilner, D. J. 1997, ApJ, 489, 719
McKee, C. F., & Ostriker, E. C. 2007, ARA&A, 45, 565M
McKee, C. F., & Tan, J. C. 2003, ApJ, 585, 850
Mendes, M. B., Buhr, H., Berg, M. H., et al. 2012, ApJ, 746L, 8M
Molinari, S., Brand, J., Cesaroni, R., & Palla, F. 1996, A&A, 308, 573
Molinari, S., Brand, J., Cesaroni, R., & Palla, F. 2000, A&A, 355, 617
Motte, F., Andre, P., & Neri, R. 1998, A&A, 336, 150
Myers, P. C., Mardones, D., Tafalla, M., Williams, J. P., & Wilner, D. J. 1996, ApJL, 465, L133
Purcell, C. R., Balasubramanyam, R., Burton, M. G., et al. 2006, MNRAS, 367, 553
Rathborne, J. M., Jackson, J. M., & Simon, R. 2006, ApJ, 641, 389
Reiter, M., Shirley, Y. L., Wu, J., et al. 2011a, ApJ, 740, 40
Reiter, M., Shirley, Y. L., Wu, J., et al. 2011b, ApJS, 195, 1
Rygl, K. L. J., Wyrowski, F., Schuller, F., & Menten, K. M. 2013, ApJ, 549, A5
Shu, F. H. 1977, ApJ, 214, 488
Simon, R., Jackson, J. M., Rathborne, J. M., & Chambers, E. T. 2006a, ApJ, 639, 227
Simon, R., Rathborne, J. M., Shah, R. Y., Jackson, J. M., & Chambers, E. T. 2006b, ApJ, 653, 1325
Smith, R. J., Shetty, R., Beuther, H., Klessen, R. S., & Bonnell, I. A. 2013, ApJ, 771, 24
Sridharan, T. K., Beuther, H., Schilke, P., Menten, K. M., & Wyrowski, F 2002, ApJ, 566, 931
Thompson, M. A., Hatchell, J., Walsh, A. J., Macdonald, G. H., & Millar, T. J. 2006, A&A, 453, 1003
van der Tak, F. F. S., Müller, H. S. P., Harding, M. E., & Gauss, J. 2009, A&A, 507, 347
Wood, D. O. S., & Churchwell, E. 1989, ApJS, 69, 831
Wu, J., & Evans, N. J. 2003, ApJL, 592, L79
Wu, J., Evans, N. J., II, Shirley, Y. L., & Knez, C. 2010, ApJS, 188, 313
Wu, Y., Henkel, C., Xue, R., Guan, X., & Miller, M. 2007, ApJL, 669, L37
Zinnecker, H., & Yorke, H. W. 2007, ARA&A, 45, 481